The Abdus Salam
International Centre for Theoretical Physics

United Nations
Educational, Scientific
and Cultural Organization

International Atomic
Energy Agency

H4.SMR/1775-19

"8th Workshop on Three-Dimensional Modelling of
Seismic Waves Generation, Propagation and their Inversion"

25 September - 7 October 2006

Analysis of Induced Seismicity for Stress Field Determination and Pore Pressure Mapping

F. H. Cornet

Institute de Physique du Globe de Paris
France

PAGEOPH, Vol. 145, Nos. 3/4 (1995) 0033–4553/95/040677–24$1.50 + 0.20/0

Analysis of Induced Seismicity for Stress Field Determination and Pore Pressure Mapping

F. H. CORNET[1] and YIN JIANMIN[1]

Abstract—The focal mechanisms of some one hundred microseismic events induced by various water injections have been determined. Within the same depth interval, numerous stress measurements have been conducted with the HTPF method. When inverted simultaneously, the HTPF data and the focal plane solutions help determine the complete stress field in a fairly large volume of rock (about 15×10^6 m^3). These results demonstrate that hydraulically conductive fault zones are associated with local stress heterogeneities. Some of these stress heterogeneities correspond to local stress concentrations with principal stress magnitudes much larger than those of the regional stress field. They preclude the determination of the regional stress field from the sole inversion of focal mechanisms. In addition to determining the regional stress field, the integrated inversion of focal mechanisms and HTPF data help identify the fault plane for each of the focal mechanisms. These slip motions have been demonstrated to be consistent with Terzaghi's effective stress principle and a Coulomb friction law with a friction coefficient ranging from 0.65 to 0.9. This has been used for mapping the pore pressure in the rock mass. This mapping shows that induced seismicity does not outline zones of high flow rate but only zones of high pore pressure. For one fault zone where no significant flow has been observed, the local pore pressure has been found to be larger than the regional minimum principal stress but no hydraulic fracturing has been detected there.

Key words: Induced seismicity, stress determination, stress heterogeneity, fluid flow, fault morphology.

1. Introduction

The injection of water in a fractured rock mass generates some seismicity when the injection pressure becomes large enough (e.g., PEARSON, 1981; NIITSUMA *et al.*, 1982; CORNET *et al.*, 1982; PINE and BATCHELOR, 1984; TALEBI and CORNET, 1987; HOUSE, 1987; FEHLER, 1989). In most cases this microseismicity is caused by shear events generated by the decrease in effective normal stress, supported by pre-existing fracture surfaces. This decrease in effective normal stress is caused by the increase in interstitial pressure induced by water injection.

In this paper, attention focuses on an analysis of focal plane solutions of microseismic events induced by various water injections in a granite rock mass. This

[1] Département de Sismologie, Institut de Physique du Globe de Paris, 4 place Jussieu, 75252 Paris cedex 05, France.

analysis concerns first the possibility of using focal mechanisms for determining the regional stress field. Results obtained with a stress determination method, which integrates hydraulic test data and focal plane solutions, are discussed.

This regional stress field determination, combined with the identification of the proper fault plane for each of the consistent focal mechanisms, helps constrain the friction coefficient and the effective stress law which control the stability of this rock mass. These values provide means to map the fluid pressure away from the injection well within two fault structures which exhibit different hydraulic connection patterns.

2. Injection Tests at Le Mayet de Montagne

The granite test site at Le Mayet de Montagne, located in central France some 25 km to the southeast of Vichy, has been developed for conducting large-scale *in situ* experiments on forced water circulation (CORNET, 1989). The first deep borehole, INAG III-8, reaches 780 m, while the second one, INAG III-9, is 840 m deep and located 100 m away. Preliminary injection tests were run in these wells at flow rates equal to 8.6 l/s in order to identify the main flowing zones in the lowest 250 m from the bottom of the wells. In INAG III-9 only four significant flowing zones have been identified. The upper one occurs around 650 m.

During the early stage of the reservoir development, a small-scale circulation test was conducted between the two boreholes. Water was injected through the 250 m open hole section at the bottom of INAG III-9, with a 8.3 l/s injection flow rate and a 8.2 MPa well head pressure, for about 70 hours. At the end of this circulation test, the production well (INAG III-8) was shut off while injection proceeded for another 3 hours at 22.2 l/s (12 MPa well head pressure).

During this preliminary reservoir development, the induced seismicity was monitored with a network of fifteen 3D seismic stations. *P*- and *S*-wave velocities were determined by detonating small charges of dynamite at various depths in the two deep wells as well as in some superficial ones so as to cover various azimuths and the entire depth range in which events were expected. These blasts were also favorably utilized to determine the orientation of the horizontal components of the seismic stations. The velocity field identified in this manner has been found to be fairly anisotropic and this anisotropy has been taken into account in locating events (TALEBI and CORNET, 1987). About 100 events were recorded during the small-scale circulation experiment, from which 31 well-defined focal mechanisms could be computed (CORNET and JULIEN, 1989; see also Table 1).

The large-scale reservoir development involved three phases during which the induced microseismicity was continuously monitored by the previously mentioned network. During the first phase, injection proceeded through INAG III-8 between the bottom of the well and an inflatable packer set at 713 m. Two inflatable packers

Table 1

Location and focal plane solutions for the microseismic events observed during the initial reservoir development. Events 100, 101 and 102 were observed during initial stimulations in the well INAG III-8 while all the others correspond to injections in the well INAG III-9. Origin of coordinates is on the INAG III-8 well head. For the nodal planes, d is azimuth and p is dip while i is rake. δ and ε refer to standard deviations of the parameter shown as index

No.	X (east)	Y (north)	Z (downward)	First nodal plane						Second nodal plane					
				(d1,	p1,	i1)	(δd1,	δp1,	δi1)	(d2,	p2,	i2)	(δd2,	δp2,	δi2)
1	87 ± 7	−56 ± 4	850 ± 13	266	66	48	30	7	20	150	48	146	20	3	15
2	68 ± 8	−96 ± 8	640 ± 8	342	78	223	12	4	7	240	48	343	12	5	8
7	92 ± 7	−108 ± 1	664 ± 10	96	32	226	7	5	6	326	67	294	7	4	6
8	88 ± 7	−101 ± 5	655 ± 8	356	58	237	10	5	10	226	45	310	10	6	12
12	71 ± 8	−56 ± 10	656 ± 8	183	71	199	10	2	5	87	72	340	14	4	3
14	95 ± 5	−37 ± 2	532 ± 2	120	84	36	5	2	5	25	55	173	1	5	3
15	55 ± 2	−78 ± 3	770 ± 13	172	80	230	4	2	3	70	40	345	4	2	2
21	63 ± 15	−58 ± 4	830 ± 15	339	58	21	11	4	4	237	72	146	11	3	5
23	75 ± 8	−42 ± 2	823 ± 13	354	79	205	2	1	6	258	65	347	2	6	1
24	55 ± 3	−142 ± 3	478 ± 6	209	88	238	15	4	6	115	32	356	15	4	6
26	95 ± 2	−107 ± 2	668 ± 9	194	84	40	3	2	5	99	50	172	4	5	2
27	67 ± 3	−50 ± 2	831 ± 13	180	89	224	2	2	2	90	46	359	2	2	2
29	87 ± 6	−122 ± 6	660 ± 15	78	65	188	1	5	2	346	82	335	3	1	5
31	75 ± 3	−40 ± 4	800 ± 6	182	70	203	1	4	2	85	68	339	2	2	4
32	98 ± 3	−108 ± 5	770 ± 15	160	75	221	6	2	6	56	45	339	6	3	3
33	92 ± 3	−64 ± 3	763 ± 12	142	86	220	8	2	3	48	50	355	9	2	3
34	50 ± 0	−100 ± 5	950 ± 10	22	81	181	1	1	1	291	89	352	1	1	1
38	75 ± 2	−62 ± 8	798 ± 5	140	85	220	9	2	2	46	50	354	11	2	2
43	52 ± 3	1 ± 3	520 ± 12	248	42	56	10	9	27	108	56	116	20	7	25
45	86 ± 2	−109 ± 4	653 ± 4	242	88	54	10	2	3	150	36	177	13	2	5
49	66 ± 4	11 ± 5	486 ± 10	296	74	24	3	2	3	199	68	163	1	3	2
51	61 ± 3	12 ± 4	509 ± 9	243	48	18	5	13	3	142	76	136	5	2	7
52	61 ± 1	−49 ± 2	449 ± 5	72	79	38	2	2	2	334	54	167	2	2	2
55	73 ± 3	−66 ± 3	816 ± 11	170	84	225	5	2	2	74	46	350	7	2	2
58	61 ± 2	25 ± 3	482 ± 11	256	46	35	5	7	10	140	66	131	5	5	8

Continued overleaf

Table 1 (*Contd.*)

No.	X (east)	Y (north)	Z (downward)	First nodal plane ($d1$,	$p1$,	$i1$)	($\delta d1$,	$\delta p1$,	$\delta i1$)	Second nodal plane ($d2$,	$p2$,	$i2$)	($\delta d2$,	$\delta p2$,	$\delta i2$)
59	55 ± 2	-29 ± 3	825 ± 10	160	80	223	8	4	2	60	48	346	8	4	5
61	87 ± 1	-5 ± 8	555 ± 17	50	50	185	1	1	3	317	88	320	5	4	1
62	101 ± 3	-12 ± 14	770 ± 30	324	77	211	13	4	4	224	60	344	3	4	4
66	83 ± 1	-84 ± 2	521 ± 6	324	80	231	14	4	5	221	40	344	14	5	5
69	80 ± 2	-69 ± 3	477 ± 5	340	72	261	6	2	2	185	20	293	21	10	20
70	74 ± 3	-2 ± 4	512 ± 6	230	50	12	5	4	2	132	80	140	3	3	5
71	71 ± 3	-50 ± 3	827 ± 3	168	81	221	5	2	4	70	50	349	6	3	3
100				305	69	61				195	48	140			
101				325	68	8				233	85	149			
102				330	68	15				236	80	149			

were also placed in INAG III-8 in order to limit as much as possible short circuits caused by the well. Injection proceeded for 210 hours at a flow rate equal to 8.3 l/s with a well head pressure which varied from 7.5 MPa at the beginning of the test to 9.1 MPa (stabilized value at the end of the test). Only two microseismic events were observed during this phase. Thereafter the injection flow rate was increased to 16.7 l/s with a well head pressure reaching 10.8 MPa (total injected volume of 11 665 m^3). During this phase eleven microseismic events were monitored, ten of which yielded clear fault plane solutions (Table 2).

During the second phase, injection proceeded through the 250 m long open hole section at the bottom of INAG III-9 at a flow rate equal to 8.3 l/s with a well head pressure equal to about 9.2 MPa. A stationary condition was reached after one week of injection. This stationary condition was maintained for about 21 days so that the total injected volume for this phase reached 14 790 m^3. During this phase, 50 microseismic events were recorded from which 23 yielded well-defined focal mechanisms (Table 2).

The third phase (injection between 600 m and 840 m in INAG III-9) involved a first period designed for characterizing the hydraulic properties of the system while the second period was run for testing long duration stationary circulation conditions. During the first period the system was tested for various flow rates. Each flow rate was maintained constant for periods ranging from 5 to 3 days. The maximum flow rate reached 21.1 l/s with a well head pressure equal to 12.5 MPa after three days of pumping, then the flow rate was decreased to 16.6 l/s. During this third period 46 microseismic events were recorded from which 19 yielded a well-defined focal mechanism (Table 2). No event was recorded during the pumping tests at flow rates smaller than, or equal to, 8.3 l/s (well head pressures smaller than 9.3 MPa). All events occurred during the initial period of this phase except for one event which occurred just before the end of pumping, when the flow rate had been increased to 12.5 l/s (well head pressure equal to 10.2 MPa) and another one occurred when pumping had stopped. The total injected volume during the first period of this phase reached 16 310 m^3.

Thus, while the seismic activity monitored during the early reservoir development (about one hundred events) corresponds to a total injected volume of about 2200 m^3, the various seismically active phases (11 events, 50 events, 46 events) associated with the large-scale injection tests correspond to injected volumes ranging from 11 665 m^3 to 16 310 m^3. The location of all events recorded while injection was proceeding through the well INAG III-9 are shown on Figure 1.

The duration of most events ranges between 0.3 and 0.5 seconds, with the largest ones reaching 0.6 s. The P-wave corner frequencies vary between 200 and 400 Hz while the seismic moments vary between 10^7 and 10^8 Nm. Accordingly, the magnitudes of these events range between -2 and -1.

Three main active zones can be identified in Figure 1: a deeper zone, in which no clear structure has been identified, and two subplanar structures. CORNET and

Table 2

Location and focal plane solutions for the microseismic events observed during the large-scale injection tests. Coordinate system is centered on the well head of INAG III-8. For the nodal planes d is azimuth and p is dip, i is rake; ε and δ refer to the standard deviation of the parameter shown as index

				First nodal plane						Second nodal plane					
No.	*X*(east)	*Y*(north)	*Z*(down)	(*d*1,	*p*1	*i*1)	(δ*d*1,	δ*d*1,	δ*d*1)	(*d*2,	*p*2,	*i*2)	(δ2,	δ*p*2,	δ*i*2)
2	21 ± 7	51 ± 16	803 ± 3	28	75	196	5	4	3	294	75	345	5	2	4
3	22 ± 6	50 ± 5	757 ± 15	121	70	184	6	2	3	30	86	340	7	3	2
4	22 ± 1	−124 ± 7	557 ± 10	326	80	227	5	2	6	225	44	345	8	5	4
5	22 ± 3	−118 ± 4	553 ± 2	49	85	2	5	3	3	319	88	175	5	3	3
6	23 ± 2	−248 ± 3	428 ± 6	34	70	11	4	3	10	300	80	160	6	9	3
7	166 ± 8	78 ± 2	849 ± 7	28	77	206	6	5	4	292	65	346	8	3	5
8	91 ± 14	−14 ± 4	505 ± 8	324	80	190	3	3	3	232	80	350	4	2	3
9	5 ± 6	−254 ± 2	385 ± 8	53	80	20	5	2	6	319	70	169	6	6	3
10	46 ± 3	1 ± 2	464 ± 12	356	70	190	5	5	2	262	80	340	3	1	5
11	32 ± 4	−109 ± 5	562 ± 25	76	82	16	3	2	2	344	74	172	5	2	3
13	26 ± 4	−131 ± 3	601 ± 3	344	88	212	3	2	7	253	58	358	5	7	2
15	70 ± 3	−45 ± 1	494 ± 7	332	85	202	4	2	3	240	68	355	5	3	3
16	83 ± 4	−67 ± 9	439 ± 12	350	88	18	2	2	2	259	72	178	4	2	2
17	100 ± 5	−51 ± 3	523 ± 3	22	70	219	4	2	9	277	54	335	10	7	6
19	14 ± 15	−68 ± 5	858 ± 13	296	70	191	3	5	2	202	80	336	4	1	5
20	69 ± 2	−42 ± 4	498 ± 14	348	78	201	6	2	3	254	70	347	8	3	3
21	100 ± 10	−100 ± 2	798 ± 2	284	72	186	4	4	2	192	84	342	3	2	5
23	73 ± 6	−74 ± 4	416 ± 1	83	78	14	7	2	2	350	76	168	6	2	2
24	99 ± 10	−56 ± 9	813 ± 7	141	86	206	4	2	3	49	64	356	3	3	2
26	96 ± 6	5 ± 10	500 ± 18	254	50	27	6	4	5	146	70	137	10	2	4
29	129 ± 5	−61 ± 8	563 ± 22	26	70	32	4	2	6	284	60	157	7	5	3
31	93 ± 2	−89 ± 4	839 ± 6	140	85	205	3	2	5	48	65	355	4	5	2
34	103 ± 9	−65 ± 3	566 ± 12	311	88	207	7	2	2	220	63	358	8	2	3
35	106 ± 7	−53 ± 5	567 ± 8	320	75	196	3	2	3	226	75	345	5	2	3
36	114 ± 11	−93 ± 6	795 ± 7	286	79	185	3	5	2	195	85	349	4	2	5
38	114 ± 2	−47 ± 5	554 ± 7	80	82	36	5	2	5	344	55	170	8	4	3
40	122 ± 1	−167 ± 7	621 ± 10	29	68	11	4	1	10	295	80	158	7	9	2

41	84 ± 2	-15 ± 1	566 ± 5	250	90	330	4	2	6	340	60	180	4	6	3
42	45 ± 5	-90 ± 3	804 ± 9	360	90	348	2	2	4	90	78	180	3	4	2
46	75 ± 1	10 ± 2	492 ± 6	342	86	198	3	1	3	251	72	355	5	3	2
48	119 ± 14	-74 ± 12	913 ± 16	165	75	202	7	4	4	69	69	344	6	2	4
51	78 ± 14	20 ± 8	294 ± 12	82	43	62	5	2	10	298	53	114	11	2	10
56	55 ± 5	-29 ± 4	847 ± 9	168	82	217	3	2	3	72	53	350	5	3	3
64	93 ± 8	-19 ± 7	530 ± 3	345	84	188	5	2	3	254	82	354	6	3	2
65	72 ± 3	8 ± 4	501 ± 23	268	76	24	3	2	5	172	67	165	5	4	3
67	76 ± 3	-19 ± 2	806 ± 10	296	68	185	4	5	1	204	85	338	6	1	5
71	93 ± 6	-75 ± 4	548 ± 6	356	78	201	6	1	7	262	70	347	7	6	2
76	84 ± 2	-17 ± 2	485 ± 8	336	80	200	4	2	3	242	70	349	7	3	2
78	104 ± 12	-56 ± 3	568 ± 9	332	84	212	5	2	5	238	58	353	7	5	4
80	105 ± 9	-57 ± 2	831 ± 4	314	80	210	6	3	4	218	60	348	8	4	4
83	77 ± 4	-12 ± 2	483 ± 8	334	86	202	3	2	3	242	68	356	4	3	3
88	123 ± 8	-83 ± 2	369 ± 15	133	90	57	5	4	3	43	33	180	5	3	7
90	97 ± 2	-59 ± 11	568 ± 10	336	85	194	7	2	3	245	76	355	8	2	3
92	30 ± 2	-77 ± 4	401 ± 4	33	64	205	5	2	7	292	68	332	9	6	4
93	96 ± 8	-53 ± 1	564 ± 2	121	75	182	5	2	3	31	88	345	5	2	2
94	82 ± 3	-32 ± 5	939 ± 6	264	75	180	5	5	1	174	90	345	5	1	5
95	129 ± 6	-100 ± 4	801 ± 4	18	64	202	8	4	7	278	70	332	8	5	5
96	81 ± 5	-64 ± 3	853 ± 25	290	75	188	5	5	3	198	82	344	5	2	5
97	103 ± 9	4 ± 4	870 ± 3	304	84	204	4	1	5	211	66	353	5	5	2
98	98 ± 3	-72 ± 7	528 ± 8	236	42	8	7	5	6	140	85	132	6	2	5
102	101 ± 5	-62 ± 4	558 ± 9	298	86	201	4	2	3	207	69	356	5	3	3
105	103 ± 11	-64 ± 4	568 ± 7	298	85	202	4	1	3	206	68	355	5	3	2

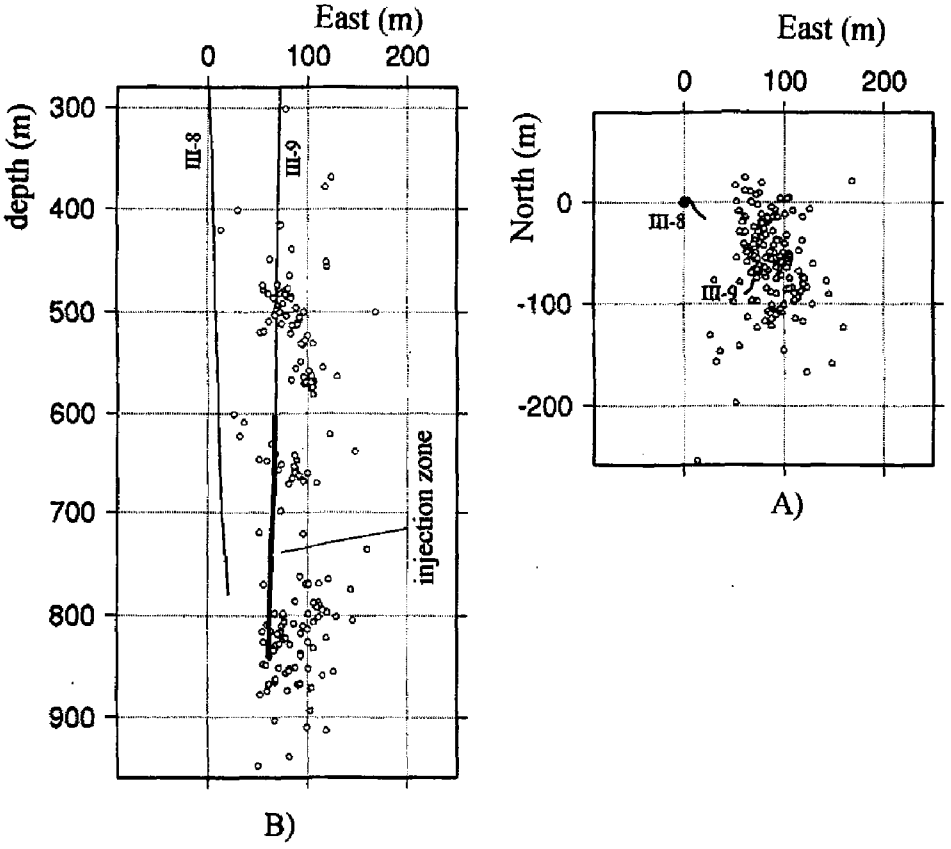

Figure 1
Location of all events recorded while injection was proceeding through the well INAG III-9. A) Projection on a horizontal plane, B) Projection on a vertical plane oriented in the east-west direction. Injection was conducted between 598 m and 840 m.

SCOTTI (1993) identified by a least-squares technique the best fitting planes passing through the upper and lower planar structures. The upper seismic zone fits with a plane oriented N 04°E and dipping 61° to the east. It intersects the well INAG III-9 in the 481–521 m depth range. The lower planar structure has been fitted with a plane oriented N 174°E and dipping 36° to the east. It intersects the well INAG III-9 in the depth range 630–654 m. Within both these depth intervals sonic logs outline zones of alterations, confirmed by the analysis of the cuttings produced during drilling operations.

Interestingly, none of these orientations could be identified from a statistical analysis of the fractures identified by borehole imaging within these depth intervals. Yet it is one of the dominant fault orientations mapped on site. This demonstrates that the small-scale morphology of a fractured (fault) zone does not always reflect its large-scale geometry and that fault zones may involve small-scale fractures of very diverse orientations. Also, while both zones are clearly visible on the geophysical logs and in the cuttings, only those around 650 m exhibit a significant hydraulic conductivity: The zone intersected around 500 m does not appear on the initial flow

logs and therefore is not connected to the large-scale hydraulically significant fracture network (CORNET and SCOTTI, 1993).

3. Determination of the Regional Stress Field

The regional stress field has been determined by three different methods: The Hydraulic Tests on Pre-existing Fractures (HTPF) method, the inversion of focal mechanisms of induced seismicity, the simultaneous inversion of HTPF data and focal plane solutions. These results have already been published (CORNET and JULIEN, 1989; CORNET *et al.*, 1992; YIN and CORNET, 1994). They are briefly recalled here for later discussions.

3.1 The HTPF Stress Determination

The HTPF method consists of conducting hydraulic tests on pre-existing fractures of known orientation (characterized by the normal $\mathbf{n}$ to the fracture plane) for determining the normal stress σ_n supported by the fracture plane. The problem is to determine the six components of the stress σ such that $\sigma\mathbf{n} \cdot \mathbf{n} = \sigma_n$. The regional stress field σ is presumed to vary linearly with the spatial coordinates (x_1, x_2, x_3; x_1 horizontal, positive to the north, x_2 horizontal, positive to the east, x_3 vertical, positive downward):

$$\sigma = \mathbf{S} + x_1\alpha^1 + x_2\alpha^2 + x_3\alpha^3 \tag{1}$$

where $\mathbf{S}$, α^1, α^2, α^3 are symmetrical tensors. α^1, α^2, α^3 are the stress gradients respectively in the x_1, x_2, x_3 directions. Equilibrium conditions show that, in the absence of topography or lateral heterogeneities ($\alpha^1 = \alpha^2 = 0$), one of the principal directions of α^3 is vertical (CORNET, 1992). This result is very similar to that proposed by MCGARR (1980) except that, here, no assumption is made regarding the constitutive equation of the rock mass. It is only assumed that, within the domain of interest, the stress field varies fairly smoothly around some central point so that its components can be approximated by linear functions. From now on the tensor α^3 will be simply denoted by α. The stress determination consists of determining $\mathbf{S}$ and α derived from N HTPF data. A HTPF datum includes both the normal stress measurement and the fracture orientation determination.

At Le Mayet de Montagne, eighteen HTPF measurements have been conducted between 60 m and 730 m, prior to the water circulation experiments. For this stress determination the regional stress field and its first derivative are assumed continuous up to ground surface. The solution is defined by the principal values of $\mathbf{S}$($S_1 = 5.1$ MPa, $S_2 = 0.2$ MPa, $S_3 = 0$; S_1 is horizontal and oriented N 24°E.) and α($\alpha_1 = 0.0226$ MPa/m; $\alpha_2 = 0.0084$ MPa/m; $\alpha_3 = 0.0264$ MPa/m; α_1 is oriented 104°

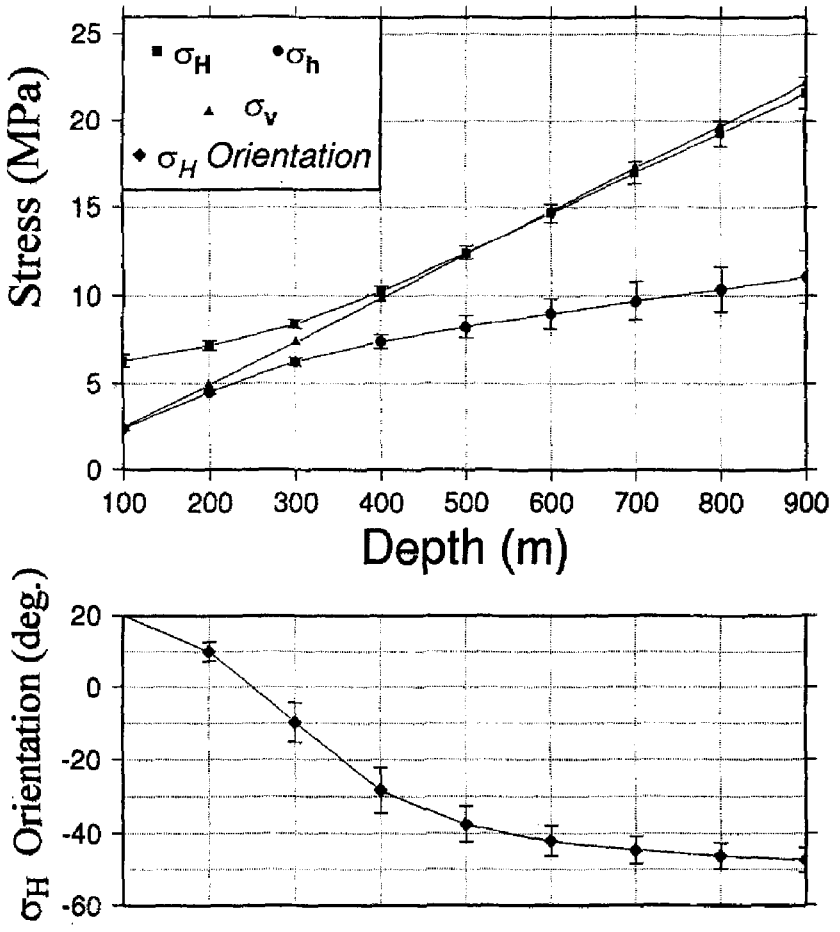

Figure 2
Stress profiles derived from the HTPF measurements conducted prior to the injection tests. σ_H orientation is measured from the north and positive eastward.

to the north of S_1). Values for the horizontal principal stress magnitudes σ_H and $\sigma_h(\sigma_H > \sigma_h)$ and for the orientation of σ_H with respect to north (positive eastward) are indicated for various depths in Figure 2.

Two and a half years after the main water circulation experiment was completed, another 13 HTPF measurements have been carried out in well INAG III-9. These measurements demonstrate that no permanent large-scale stress perturbation has been induced by the various water injections (CORNET 1992). It has been observed, however, that two of these HTPF measurements (at 780 m and 773 m) are heterogeneous with respect to the original regional stress field and that, according to a spinner log, these heterogeneous data are located close to one of the most hydraulically significant zones of the borehole.

3.2 Integration of Focal Solutions in the Stress Determination

A few authors (e.g., VASSEUR *et al.*, 1983; GEPHART and FORSYTH, 1984; JULIEN and CORNET, 1987; RIVEIRA and CISTERNAS, 1990) have proposed deter-

mining the regional stress field from an inversion of the focal plane solutions of seismic events. These determinations asssume that the stress field is uniform throughout the volume in which the seismic events occurred and that the slip vector is parallel to the resolved shear stress supported by the slipping planes (WALLACE, 1951; BOTT, 1959). Because only the direction of the shear component is constrained (and not its magnitude), these stress determinations yield only the principal stress directions (defined by the Euler angles ϕ, ψ and θ where ϕ and ψ are respectively the azimuth and dip of σ_1 and θ is the angle between the σ_2 direction and the horizontal plane) and a factor R characteristic of the ellipticity of the tensor: $R = (\sigma_2 - \sigma_1)/(\sigma_3 - \sigma_1)$; $(\sigma_1 > \sigma_2 > \sigma_3)$.

CORNET and JULIEN (1989) attempted a first stress determination with the focal mechanisms of the microseismic events observed during the preliminary reservoir development (injection of 2200 m^3). In order to satisfy the hypothesis of stress uniformity, they considered three different depth ranges: an upper one (above 550 m), an intermediate one (between 750 m and 550 m) and a lower one (below 750 m). For the two upper systems no satisfactory solution could be identified (too many inconsistent data). For the deeper system, 14 well-defined focal mechanisms were available for the inversion. Results establish that the maximum principal stress is vertical, but the maximum horizontal principal stress is oriented 70° to the east of the HTPF solution ($\varphi = 329°$, $\psi = 79°$, $\theta = 24°$, $R = 0.55$; Figure 3). This solution is consistent with 12 of the 14 mechanisms.

Another stress determination (YIN, 1994) has been undertaken with the complete set of focal mechanisms (seismicity induced by the large-scale injections combined with that of the early reservoir development). Here again the data has been separated into three different depth ranges in order to satisfy the stress homogeneity hypothesis. Although the resolution is not very good, results are far more satisfactory than Cornet and Julien's solution. For the deeper seismic system (Fig. 4), the solution yields $\varphi = 354°$, $\psi = 46°$, $\theta = 92°$, $R = 0.32$. For all depth

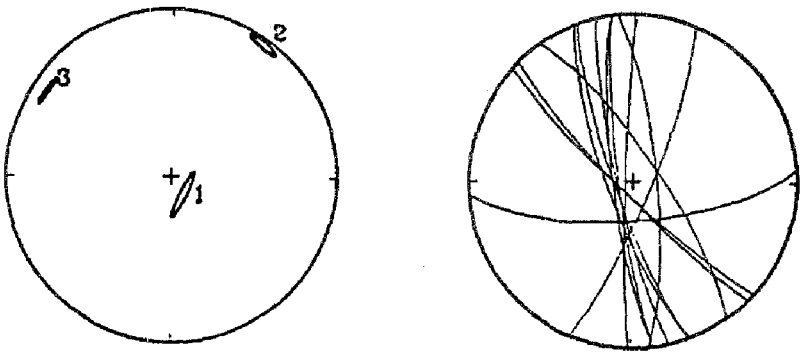

Figure 3
Stress determination derived from the inversion of focal mechanisms of the microseismic events observed during the preliminary reservoir development (total injected volume of 2200 m^3). Only the deepest seismic domain (see Fig. 1B) is considered. The stereographic projection of the principal directions is shown on the left. The orientation of selected planes is shown on the right.

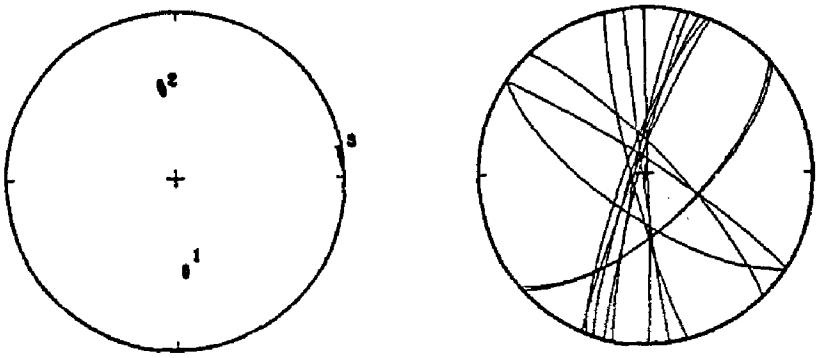

Figure 4
Same as Figure 3 but the seismic events considered are those induced by the large-scale reservoir development (injected volumes of 14 790 m^3 and 16 310 m^3).

ranges, a systematic 20 to 30 degrees discrepancy is observed for the maximum horizontal principal stress orientation, as determined on the one hand with this focal plane inversion and on the other hand with the HTPF method.

While the HTPF solution remains stable when new data are introduced, the focal plane solution varies, depending on the set of data considered for the inversion. As mentioned above, the post-circulation HTPF measurements outlined zones of local stress heterogeneity associated with some of the main flowing zones. Thus it has been concluded that some of the focal mechanisms are very likely "polluted" by local stress heterogeneities, and these, in turn, influence the stress determination.

However, the HTPF measurements involve only subvertical fractures, resulting in very poor resolution on the vertical stress component. Further, the HTPF stress determination assumes that the stress field is continuous up to the surface and that the vertical direction is principal at all depths. In order to alleviate these limitations and take advantage of those focal mechanisms which are not influenced by local stress heterogeneities, a joint inversion method integrating the HTPF data and the focal mechanisms has been developed (YIN and CORNET 1994). In this inversion scheme the stress field is represented by ten parameters. In equation (1), the tensor **S** represents the stress at a given depth; none of its six components (the three principal values S_1, S_2 and S_3 and the three Euler angles λ_1, λ_2 and λ_3) is assumed *a priori* to be null. The tensor α is the vertical stress gradient around this depth and lateral stress variations are presumed to be negligible within the domain of interest. Equilibrium conditions impose that α exhibits a vertical principal direction so that it is described by 4 parameters. The inversion scheme uses a genetic algorithm to identify the optimal solution and a Monte Carlo method to estimate the uncertainty of the determination.

This integrated stress determination has been conducted with all the focal mechanisms available for the site (including those found to be heterogeneous with HTPF stress determination) and with HTPF data obtained within the same depth

interval as that of the focal mechanisms (all data obtained above 250 m have not been included). Further, the two deep HTPF measurements conducted close to a fracture zone which had been identified as being heterogeneous, have also been disregarded. This provides 87 focal mechanisms and 22 HTPF measurements.

Results of the joint inversion yields for **S** (defined at 750 m): $S_1 = 20$ MPa, $S_2 = 19.4$ MPa and $S_3 = 11.8$ MPa, $\lambda_1 = -34°$, $\lambda_2 = 86°$ and $\lambda_3 = 88°$. The principal values for the vertical gradient are $\alpha_1 = 0.0226$ MPa/m, $\alpha_2 = 0.0084$ MPa/m; $\alpha_3 = 0.0264$ MPa/m (in the vertical direction); the orientation of α_1 with respect to the north is $\eta = \text{N162°E}$.

The stress field and its uncertainty are shown on Figure 5 for various depths. The maximum principal stress was found to be vertical below 700 m and is equal to the weight of overburden as determined from the rock density (0.026 MPa/m). Also, the orientation of the maximum horizontal principal stress is very close to that determined with the sole HTPF measurements.

The misfit between a given fault plane and a given stress tensor is characterized by the rotation which must be applied to the fault plane in order to bring the resolved shear stress supported by the fault parallel to the slip vector observed for this plane. A focal plane is considered inconsistent with a given tensor when its misfit is larger than three times the standard deviation associated with the plane orientation determination. The results obtained from the joint inversion are consistent with 21 of the HTPF measurements and 70% of the focal plane solutions. This clearly shows that a few microseismic events occur in zones of stress heterogeneity.

Given the observation mentioned earlier that fault zones involve small-scale fractures of very diverse orientation, it may be anticipated that locally, along the fault plane, the stress is very heterogeneous with respect to the regional stress field. Spectral analysis of the *P* waves for the microseismic signals reveals corner frequencies in the 200–500 Hz range (TALEBI and CORNET, 1987). Thus, the mean size of these events is estimated to stand somewhere between 0.5 and 5 m. This suggests that the rock volume affected by the stress heterogeneities causing the discrepancy between the observed slip plane and the estimated resolved shear stress, is of the same order of magnitude.

4. Identification of Stress Heterogeneities near Fault Zones

In order to easily conduct stress determination with the HTPF technique, MOSNIER and CORNET (1989) have developed a tool (the HTPF tool) combining an electrical imaging function with a wireline straddle packer. The electrical imaging function is used first to identify pre-existing fractures of various dip and azimuth in the borehole. Next, the straddle packer is placed precisely at the required depth, by means of real time imaging of the borehole wall, and hydraulic tests are run in order to measure the normal stress supported by these pre-existing

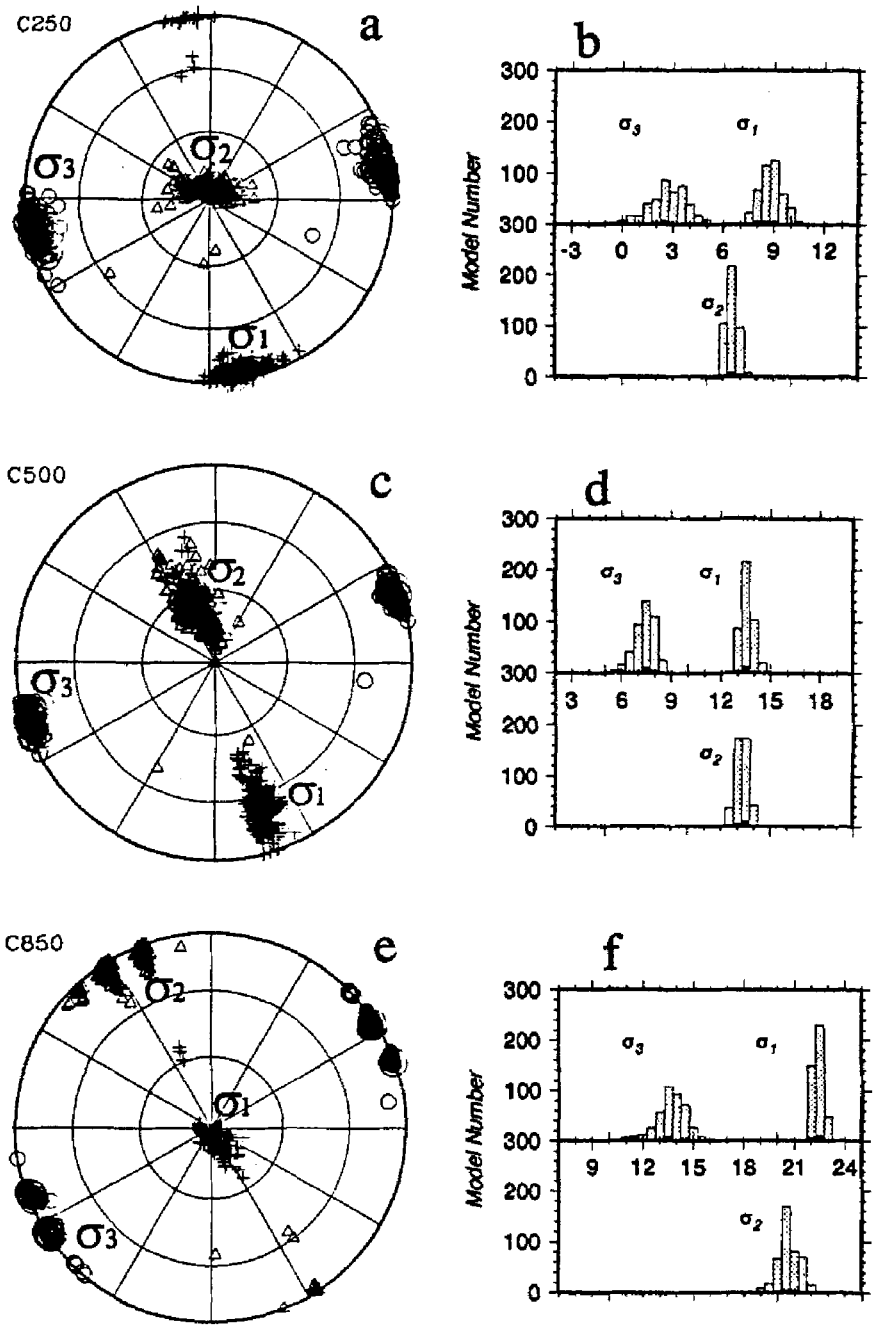

Figure 5
Stress determination obtained after integrating 22 HTPF measurements and 87 focal mechanisms. The stress field is presumed to vary linearly with depth. Results are shown at three different depths (250 m, 500 m, 850 m). a), c) and e) refer to the principal stress directions while the magnitudes (in MPa) are shown on b) d) and f). These results correspond to 430 models which are included within 95% confidence level.

fractures. This provides a unique opportunity to thoroughly investigate stress heterogeneities associated with local faults or altered zones.

As mentioned above, CORNET (1992) successfully used this technique to identify a stress perturbation in the vicinity of one of the most significant flowing zones in the well INAG III-9. SCOTTI and CORNET (1994a) analyzed two different mecha-

nisms for modelling this observed heterogeneity. The first one assumes that the fault zone can be assimilated with a soft inclusion in an otherwise stiff rock; the second one supposes that the shear stress supported by the fault plane was partially released through creep or friction. Only the second mechanism (shear stress relief) was found to be consistent with observations. Further, this mechanism was also shown to be consistent with heterogeneities identified with the focal plane solutions of induced seismicity. Thus, a new set of HTPF measurements has been undertaken in order to determine whether the stress field near the two upper planar seismic zones is also heterogeneous with the regional stress field and consistent with a local shear stress relief. Results are shown in Table 3.

In Table 3, the measured values of normal stress are compared to the values computed with the regional stress field identified by the integrated method. Given the uncertainty on the orientation of the fracture planes (about 5°), many of these results are found to be consistent with the computed regional stress. Locally, within the depth interval at which the upper planar seismic zone intersects the well, some data are found to be heterogeneous while some nearby data (less than 6 meters away) are found to be consistent. This supports the proposition that very locally the stress field near and within fault zones is heterogeneous so that focal plane solutions of induced seismicity may not be representative of the regional stress field.

However, the most striking result is the observation that between 550 m and 611 m the measured normal stress is larger than the regional maximum principal stress, in some places by as much as 10 MPa. Clearly this observation does not fit the uniform shear stress relief process proposed by SCOTTI and CORNET (1994a), but requires some locally heterogeneous slip motion. It is not clear at this point whether this heterogeneity of slip motion is associated with the spatial extension of the fault zones or if it is associated with heterogeneous slip within the faults. The quality of the data does not provide means for precisely constraining the geometry of the fault zones. Nonetheless these results do demonstrate that faults are associated locally with very heterogeneous stress distributions so that focal plane solutions may not be representative of the regional stress field.

It is concluded that, when only focal mechanisms are used to determine the regional stress field, those which are clearly inconsistent with this regional stress are easily identified by the inversion technique, but those which are only slightly inconsistent influence the solution and induce some systematic error. Hence the different results obtained with the different sets of focal mechanisms, and the systematic error observed between fault plane inversions and HTPF measurements.

It could be argued that this conclusion is only valid for focal mechanisms of induced seismicity because of the small size of the events considered for this analysis. Although this will not be further discussed here, it will be mentioned that SCOTTI and CORNET (1994b) have reached conclusions similar to those presented here above, after comparing results from various HTPF stress determinations with the focal mechanisms of natural seismic events with magnitude ranging from 3 to

Table 3

HTPF data obtained in 1994 in order to explore the stress field in the vicinity of the upper and lower planar seismic zones. x_3, ϕ, θ, σ_n are respectively the values measured for the depth, the azimuth and the dip of the normal to the fracture plane and the normal stress supported by the fracture plane. ϕ_c, θ_c, σ_{nc} are the a posteriori values for ϕ, θ, σ_n as determined by the least squares inversion procedure. ε_ϕ, ε_θ, $\varepsilon_{\sigma n}$ are the standard deviations on the measurements. $\Delta\sigma_n$ is the difference between the measured value and that expected from the integrated stress determination. When $\Delta\sigma_n$ is larger than 1 MPa, the measurement is considered heterogeneous with the regional stress field; it is not considered for the stress determination. Note the strong heterogeneity around 600 m, i.e., in between the two planar seismic zones. Since these seismic zones exhibit very strong dip, they remain fairly close to the borehole for long depth intervals.

x_3 m	ϕ	ε_ϕ	ϕ_c	θ	ε_θ	θ_c	σ_n MPa	$\varepsilon_{\sigma n}$ MPa	σ_{nc} MPa	$\Delta\sigma_n$ MPa
401	114,0	4	105,0	85,9	2	86,0	8,5	0,2	8,9	−0,4
482	115,0	4	117,0	80,1	2	80,0	12,3	0,5	11,6	0,7
501	68,7	4	73,0	89,0	2	88,9	9,6	0,2	9,3	0,3
554	132,0	4	132,6	89,1	2	89,1	14,3	0,3	14,2	0,1
558	103,2	5	118,8	88,5	2	88,4	15,3	0,4	13,7	1,6
665	196,0	4	193,0	85,5	2	85,43	12,8	0,3	12,6	0,2
678	187,0	4	179,4	85,5	2	85,3	14,8	0,3	14,4	0,4
686	180,0	4	188,6	73,3	2	74,1	13,3	0,3	13,7	−0,4
762	262,9	4	263,0	7,3	2	7,0	20,0	0,3	19,6	0,4
446	192,0			81,1			12,8	0,3	10,3	2,5
530	182,0			81,1			15,0	0,5	12,0	3,0
597	95,0			85,8			17,3	0,4	12,7	4,6
605	43,5			84,3			20,6	0,4	10,2	10,4
611	276,0			80,0			23,4	0,4	13,2	10,2
698	134,5			86,0			13,8	0,3	17,8	−5,0

4.5. Given the proposition that slip motion along faults is very heterogeneous (HERERO and PASCAL, 1994; COCHARD and MADARIAGA, 1994), it seems reasonable to anticipate that the stress field in the vicinity of fault zones is also very heterogeneous. This implies that some aftershocks of major seismic events are also very likely affected by local stress heterogeneities so that inversion of focal mechanisms of aftershocks may lead to biased stress determinations.

Further, considering the Le Mayet de Montagne results, one may wonder if the source of the heterogeneities are to be found in the morphology of the fault or simply in the heterogeneity of the slip motion along the fault. Answering this question will require some modelling which has not yet been done. Given the fact that many of the microseismic events are located a short distance from the main fault zone identified with the least-squares technique, and that most of the slip planes observed for these events are not parallel to this main fault plane, it seems very likely that morphology plays a significant role in developing the stress heterogeneities. This may

in turn induce a heterogeneous slip motion along the main fault which may further enhance these stress heterogeneities. Only modelling, in close connection with detailed mapping of the stress heterogeneities, will help resolve this question. This modelling requires an accurate description of the local pore pressure within the fault. This is discussed now.

5. *Analysis of the Consistent Focal Mechanisms for Pore Pressure Mapping*

In addition to the regional stress determination, the joint inversion of HTPF data and focal plane solutions yields two results. First it identifies those focal mechanisms which are homogeneous with the regional stress field; then for these mechanisms it selects which of the two nodal planes is the slipping plane. This can be beneficial in obtaining some estimate of the friction coefficient for this rock mass. It can also be used to map the pore pressure perturbations induced by the fluid injections.

It is often assumed that the shear strength of pre-existing fractures obeys the effective stress principle (TERZAGHI, 1945), namely that the resistance to shear depends on the difference between the total normal stress (σ_n) supported by the fractures and the fluid pressure (p_p) assumed to act on the totality of the fracture area undergoing failure ($\sigma'_n = \sigma_n - p_p$). However, it also has been proposed (ROBINSON and HOLLAND, 1970) to consider that, since the pore space corresponds to a fraction of the total fracture area, only a fraction (β) of the pore pressure is to be considered for the effective normal stress ($\sigma'_n = \sigma_n - \beta p_p$). In the present paper we have considered both possibilities ($\beta = 1$ or $\beta = 0.9$) and assumed that the shear strength of pre-existing fractures follows Coulomb's friction law, with the assumption of zero cohesion

$$|\tau| = \mu(\sigma_n - \beta p_p) = \mu\sigma'_n. \tag{2}$$

The pore pressure at the location of a microseismic event can be written $p_p = p_0 + dp$, where p_0 is the original hydrostatic pressure and dp is the increment of pressure induced by the fluid injection. This yields

$$dp = \{(\sigma_n - \beta p_0)/\beta[1 - |\tau|/\mu(\sigma_n - \beta p_0)]\}. \tag{3}$$

The value of dp can be normalized with respect to p_i, where p_i is the increment of pressure with respect to hydrostatic pressure in the injection well at the depth of injection (i.e., the well-head pressure corrected for pressure losses caused by flow through the tubing in the injection well). In the rock mass, the ratio dp/p_i varies between 1, in the vicinity of the injection hole where pre-existing fractures are opened, and 0 near the production well or near the far field boundary, where the interstitial pressure is hydrostatic. On Figure 6, β is assumed to be equal to one (standard effective stress law) and the values for dp/p_i have been plotted versus the

values of $|\tau|/\mu(\sigma_n - \beta p_0)$, first with μ equal to 1 (Fig. 6a), second with μ equal to 0.6 (Fig. 6b). It may be observed that if the friction coefficient μ becomes slightly larger than 1, then the local pore pressure increment required to induce shear would have to be larger than the injection pressure. Also, if the friction coefficient is equal to 0.6, the pressure required to induce slip for some events is about equal to hydrostatic pressure. Thus the friction coefficient is found to stand somewhere between 0.95 and 0.65, i.e., values which are fairly common for most rocks. Results shown on Figure 7 are similar to those of Figure 6 (for a friction coefficient of 0.5) except that β has been taken equal to 0.9 (the pore pressure is not acting throughout the complete area of the fracture). These results suggest that, with such an effective stress law, the pressure required to induce slip for some of the events is larger than the injection pressure. Yet for other planes, equilibrium is barely reached with hydrostatic pressure conditions. This demonstrates that for this rock mass Terzaghi's effective stress concept is satisfactory, so that the coefficient β in the effective stress law applied to friction, is equal to 1.

Now, given the stress field determined with the integrated method and given the selection of the nodal planes which results from this stress determination, the selected friction law as expressed by equation (3) may be used to map the pore pressure distribution within the rock mass. The normalized pressure increment dp/p_i has been plotted as a function of the distance between the hypocenter of the corresponding seismic event and the closest point in the injection well where water penetrates the rock formation (Figure 8). It can be seen, that for some events in the upper planar seismic zone, the pore pressure increment required to induce shear some 100 m away from the injection point is nearly equal to the injection pressure increment. This implies that either only slight flow occurs through this fracture or that its hydraulic conductivity is extremely high. As mentioned above, preliminary flow logs conducted in the well before the circulation tests, revealed that the fracture zone intersected by INAG III-9 around 500 m was taking no fluid during injection, contrary to the fault zone intersected around 650 m. Thus the large pore pressure identified by the seismic activity analysis is consistent with the flow logs conducted in the borehole: the upper planar seismic zone, although hydraulically conductive, is not connected to the main fracture network of the rock mass, but is connected to the injection well.

This mapping of the interstitial pressure in the upper seismic zone raises an intriguing question regarding the hydraulic behavior of this system. Indeed, at some places the local pore pressure is nearly equal to the injection pressure (the well-head injection pressure varies between 8.3 MPa at 8.5 l/s to 12.5 MPa at 20.8 l/s), and therefore is larger than the regional minimum principal stress magnitude in this depth interval ($\sigma_h = 7.5$ MPa at 500 m). Since stress heterogeneities are only localized, according to the good fit observed for many microseismic events, this should have resulted in the development of hydraulic fracturing. But none has been identified. Indeed, during all the injection tests a network of six tiltmeters continu-

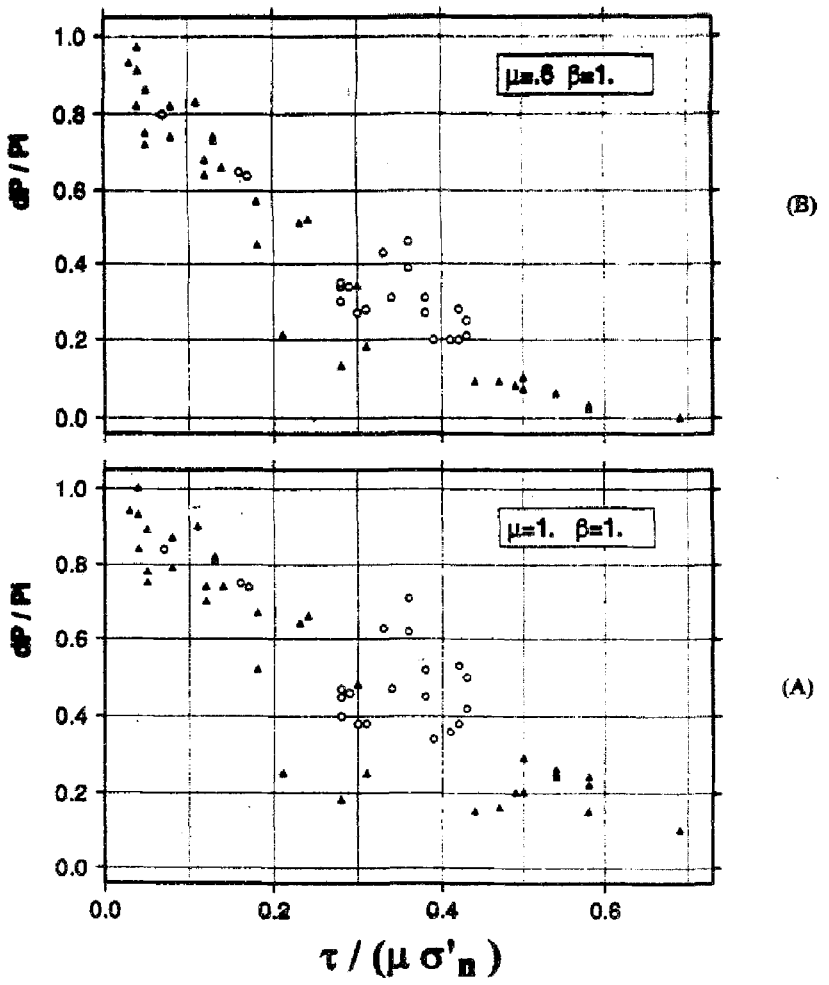

Figure 6

Calibration of the friction law controlling slippage along pre-existing fractures. On abscissa are plotted the values of the ratio between the tangential stress supported by the slip planes and the effective normal stress. On ordinate are plotted the ratio between the pressure increment required to induce slip and the injection pressure at the well head. A) The friction coefficient has been chosen equal to 1; B) The friction coefficient has been chosen equal to 0.6. In both cases the classical effective stress concept ($\beta = 1$) is assumed to be valid. Black triangles correspond to events in the upper planar seismic zone, open circles correspond to events in the lower planar seismic zone.

ously monitored the ground deformation (DESROCHES and CORNET, 1990). The absence of significant tilt during all the injection tests indicates that if any hydraulic fracture did propagate, it remained smaller than 15 to 20 m. Thus this analysis suggests that, within fault zones, the pore pressure may be significantly larger than the minimum principal stress without significant hydraulic fracturing, and this for time periods exceeding fifteen days.

The lateral extension of the lower planar seismic zone is considerably smaller than that of the upper seismic zone. Also, the pore pressure determined from the analysis of the induced seismicity is found to be substantially lower than within the upper seismic zone, and the values are decreasing regularly as the events occur

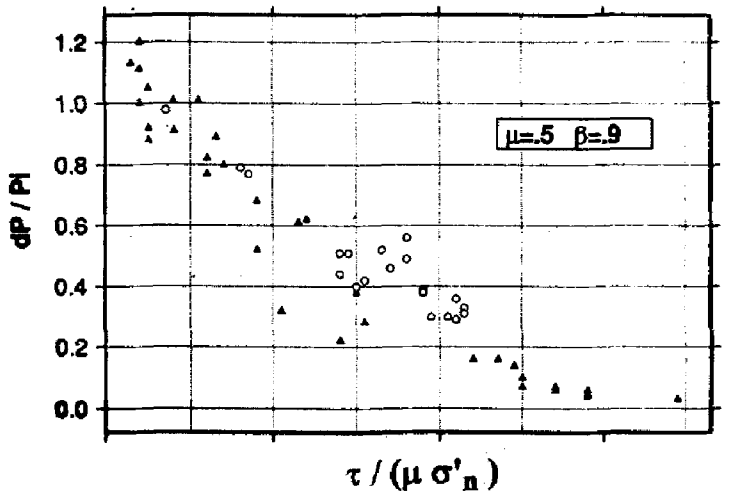

Figure 7
Same as Figure 6 but, in the effective stress law, β has been chosen equal to 0.9. Further, the friction coefficient has been chosen equal to 0.5.

further away from the well. This is consistent with the result from the flow logs which shows that this fault zone is well connected to the hydraulically significant fracture network of the rock mass.

This emphasizes the fact that induced seismicity is only representative of large pore pressure and not of large flow rate. In fact, the further away the microseismic events are from the injection well, the less likely they are to be associated with main flowing zones. Indeed, the interstitial pressure within the distant flowing zones is controlled by the far field pressure conditions and therefore, in opened systems, is too low to induce any seismicity. This is confirmed by the horizontal projection of the location of induced seismicity observed at Le Mayet de Montagne. It is observed on Figure 1 that, during injections in INAG III-9, no seismic event occured near INAG III-8 (the production well) even though the well was producing somewhere between 45% and 80% of the injection flow rate (depending on the injection flow rate). This absence of seismicity near INAG III-8 is simply linked to the low pore pressure in the vicinity of the production well.

It may be observed that none of the planar seismic zones is parallel to a principal stress direction. Thus, at least at the scale of these tests, for this granite, forced fluid flow does not occur along planes normal to the minimum principal stress but rather is controlled by a few pre-existing faults. Further, these results outline the difficulty in characterizing the hydraulic behavior of this rock mass and the shortcomings of the equivalent continuum approach: only three of four main fractures are absorbing more than 80% of the flow (BRUEL and CORNET, 1992) and these can be identified only through large-scale testing. Indeed, had straddle packer tests been conducted on the various fractures intersected by the wells, these tests would have shown that the zone around 500 m is locally hydraulically conductive

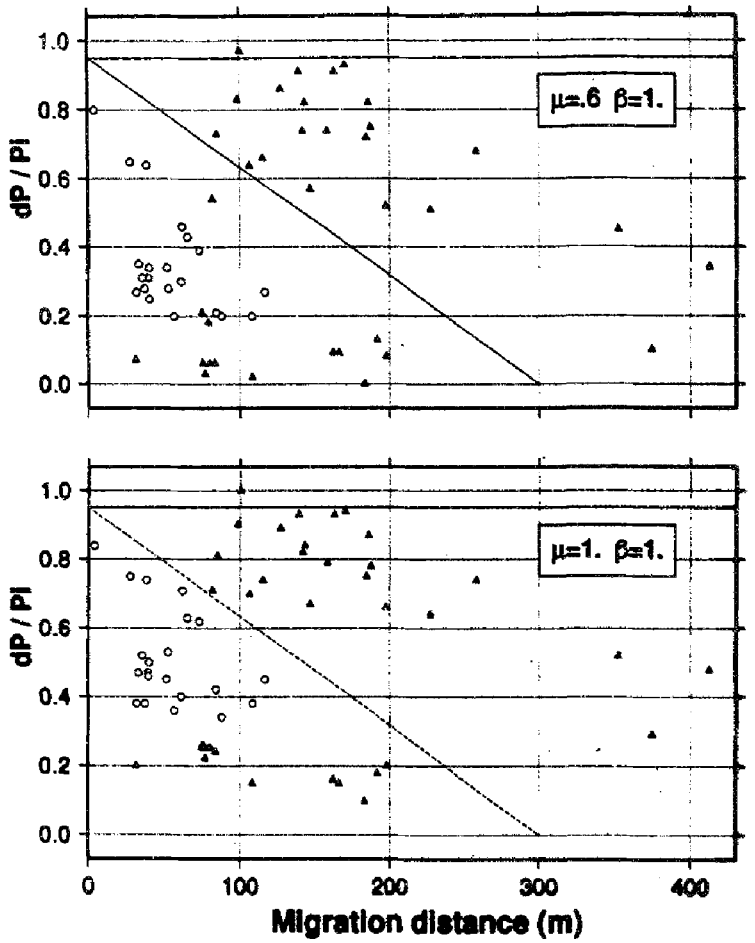

Figure 8

Mapping of the pore pressure in the rock mass during the various injections. For all focal mechanisms consistent with the integrated stress determination, the pressure increment (normalized with respect to the well-head injection pressure) required to induce slip is plotted versus the distance between the event and the closest injection point in the well (plotted in abscissa). Black triangles corrrespond to the upper planar seismic zone, the open circles refer to the lower planar seismic zone. μ is the friction coefficient, β is the corrective factor for the pore pressure in the effective stress law.

and they would have failed to identify the lack of connection at the 200 m scale. This dominance of a very limited amount of fractures on the hydraulic response of the system clearly illustrates that the concept of permeability of an equivalent continuum fails for this granite. This then raises the question of characterizing the large-scale hydraulic response of this rock mass to forced fluid flow. As shown here above, the detailed analysis of the focal plane solutions of induced seismicity, together with a sound regional stress determination, may yield part of the answer.

6. Conclusion

The mapping of seismic events induced by various water injections in this granite has shown that flow only occurs through a very limited number of fractured

zones. Some of these zones, although locally hydraulically conductive, are not hydraulically significant because they are not properly connected to the regional hydraulically significant system. All these fault structures exhibit a fairly intricate morphology so that locally the stress may be somewhat heterogeneous with respect to the regional stress field. This precludes identifying the regional stress field from the sole inversion of such locally induced focal mechanisms.

However, when combined with HTPF normal stress measurements, focal mechanisms of induced seismicity can be beneficial in efficiently constraining the regional stress field. The fact that this integrated stress determination has yielded for the Le Mayet de Montagne site a principal stress component in the vertical direction, when this was not imposed *a priori* in the inversion, is taken as a proof of the effciency of the method.

This precise regional stress determination shows that the stress heterogeneities observed along the fault zones are fairly localized and leave many portions of the fault unperturbed as demonstrated by the many consistent focal mechanisms identified within the fault zones. These numerously consistent focal mechanisms have been advantageously utilized to map the interstitial pressure. This mapping has shown that locally the pore pressure may be considerably larger than the regional minimum principal stress magnitude. Yet, no large-scale hydraulic fracture has been identified, either from the surface tilts or from the flow characteristics (a hydraulic fracture should be associated with large fluid flow, when very little has been observed in practice). The cause of this metastable situation is probably to be found in the morphology of the fault zone. This suggests that, in natural faults, the pore pressure may reach values extensively larger than the regional minimum principal stress, without inducing hydraulic fracturing, and this for a reasonably long duration (more than fifteen days in the case of Le Mayet de Montagne).

Acknowledgements

This research was supported by the European Economic Communities Directorate General XII (contract EN3G-0051-F), by Programme Interdisciplinaire de Recherche Sur l'Énergie et les Matières premières (PIRSEM) from Centre National de la Reserche Scientifique and by Agence Française pour la Maitrise de l'énergie. This work benefited greatly from the assistance of B. Bert for his technical contribution in all field work. Y. Willeveau, O. Scotti and G. Rozières assisted in some of the HTPF stress determinations.

References

Bott, B. (1959), *The Mechanics of Oblique Slip Faulting*, Geol. Mag. *96* (2), 109–117.

Bruel, D., and Cornet F. H., *Force fluid through fractured reservoirs modelling.* In *Fractured and Jointed Rock Masses* (eds. N. G. W. Cook and L. Myer) (Lawrence Berkeley Lab. Report LBL–32379, 3, 1992) pp. 519–526.

COCHARD, A., and MADARIAGA, R. (1994), *Dynamic Faulting under Rate-dependent Friction*, Pure and Appl. Geophys *142* (3/4), 419–445.

CORNET, F. H., *Experimental investigation on forced fluid flow through a granite rock mass.* In *Fourth European Geothermal Update* (eds. K. Louwrier, E. Staroste, and J. Garnish) (Kluwer Academic Pub. Dordrecht, Holland 1989) pp. 189–204.

CORNET, F. H., *In situ stress heterogeneity identification with the HTPF tool. In Rock Mechanics, Proc. 33 rd US Symposium on Rock Mechanics* (eds. Tillerson and Wawersik) (Balkema, Rotterdam 1992) pp. 39–48.

CORNET, F. H., HOSANSKI, J. M., BERNAUDAT, F., and LEDOUX, E., *Shallow depth experimentation on the concept of energy extraction from deep hot dry rocks.* In *Hydraulic Fracturing and Geothermal Energy* (eds. S. Nemat-Nasser, H. Abe, and S. Hirakawa) (Martinus Nijhoff, The Hague 1982) pp. 385–403.

CORNET, F. H., and JULIEN, Ph. (1989), *Stress Determination from Hydraulic Test Data and Focal Mechanisms of Induced Seismicity*, Int. J. Rock Mechanics Min. Sci. and Geomech. Abs. *26* (3/4), 235–248.

CORNET, F. H., YIN J., and MARTEL L., *Stress heterogeneity and flow path in a granite rock mass.* In *Fractured and Jointed Rock Masses* (eds. N. G. W. Cook, and L. Myer) (Lawrence Berkeley Lab. Report LBL-32379, vol. 1, 1992) pp. 80–87.

CORNET, F. H., and SCOTTI, O. (1993), *Analysis of Induced Seismicity for Fault Zone Identification*, Int. J. Rock Mech. Min. Sci. and Geomech. Abs. *30* (7), 789–795.

DESROCHES, J., and CORNET, F. H., *Channelling stiffness effects on fluid percolation in jointed rocks.* In *Rock Joints* (eds. N. Barton, and O. Stephanson) (Balkema, Rotterdam 1990) pp. 527–534.

FEHLER, M. C. (1989), *Stress Control of Seismicity Patterns Observed during Hydraulic Fracturing Experiments at the Fenton Hill Hot Dry Rock Geothermal Energy Site, New Mexico*, Int. J. Rock Mech. Min. Sci. and Geomech Abs. *26*, (3/4) pp. 211–219.

GEPHART, J. W., and FORSYTH, D. W. (1984), *An Improved Method for Determining the Regional Stress Tensor Using Earthquake Focal Mechanism Data: Application to San Fernando Earthquake Sequence*, J. Geophys. Res. *89* (B11), 9305–9320.

HERERO, A., and BERNARD, P. (1994), *A Kinematic Self-similar Rupture Process for Earthquakes*, Bull. Seismol. Soc. Am. *84* (4), pp. 1216–1228.

HOUSE, L. (1987), *Locating Microearthquakes Induced by Hydraulic Fracturing in Crystalline Rock*, Geophys. Res. Lett. *14*, 919–921.

JULIEN, Ph., and CORNET, F. H. (1987), *Stress Determination from Aftershocks of the Campania-Lucania Earthquake of November 23, 1980*, Ann. Geophys. *5B* (3), pp. 289–300.

MCGARR, A. (1980), *Some Constraint on Levels of Shear Stress in the Crust from Observations and Theory*, J. Geophys. Res. *85* (B11), pp. 6231–6238.

MOSNIER, J., and CORNET, F. H., *Apparatus to provide an image of the wall of a borehole during a hydraulic fracturing experiment.* In *Fouth European Geothermal Update* (eds. K. Louwrier, E. Staroste, and J. Garnish) (Kluwer Academic Pub., Dordrecht 1989) pp. 205–212.

NIITSUMA, H., NAKATSUKA, K., TAKAHASHI, H., ABE, M., CHUBACHI, N., YOKOYAMA, H., and SATO, R., *In situ AE measurements of hydraulic fracturing at geothermal fields.* In *Hydraulic Fracturing and Geothermal Energy* (eds. S. Nemat-Nasser, H. Abe, and S. Hirakawa) (Martinus Niijhoff, The Hague 1982) pp. 227–241.

PEARSON, C. (1981), *The Relationship between Microseismicity and High Pore Pressure during Hydraulic Stimulation Experiments in Low Permeability Granite Rocks*, J. Geophys. Res. *86*, 7855–7864.

PINE, R. J., and BATCHELOR, A. S. (1984), *Downward Migration of Shearing in Jointed Rock during Hydraulic Fracturing*, Int. J. Rock Mechanics Min. Sci. and Geomech. Abs. *21*, 249–263.

RICE, J. (1993), *Spatio-temporal Complexity of Slip on a Fault*, J. Geophys. Res. *98* (B6), 9885–9907.

RIVEIRA, L., and CISTERNAS, A. (1990), *Stress Tensor and Fault Plane Solutions for a Population of Earthquakes*, Bull. Seismol. Soc. Am. *80* (3), 600–614.

ROBINSON, L. H., and HOLLAND, W. E., *Some Interpretation of pore fluid effects in rock failure.* In *Rock Mechanics—Theory and Practice, Proc. 11th Symp. on Rock Mech.* (ed. W. H. Somerton) (Soc. Min. Eng., Am. Ins. Min. Met. Pet. Eng., New York 1970) pp. 585–597.

SCOTTI, O., and CORNET, F. H. (1994a), *In situ Evidence for Fluid Induced Aseismic Slip Events Along Fault Zones*, Int. J. Rock Mech. Min. Sci. and Geomech. Abs. *31* (4), 347–358.

SCOTTI, O., and CORNET, F. H. (1994b), *In situ Stress Fields and Focal Mechanism Solutions in Central France*, Geophys. Res. Lett. *21* (22), 2345–2348.

TALEBI, S., and CORNET, F. H. (1987), *Analysis of the Microseismicity Induced by a Fluid Injection in a Granite Rock Mass*, Geophys. Res. Letts. *14* (3), 227–230.

TERZAGHI, K. (1945), *Stress Conditions for the Failure of Saturated Concrete and Rock*, Proc. Am. Soc. Test Mat. *45*, 777–801.

VASSEUR, G., ETCHECOPAR, A., and PHILIP, H. (1983), *Stress State Inferred from Multiple Focal Mechanisms*, Ann. Geophys. *1*, 291–297.

WALLACE, R. E. (1951), *Geometry of Shearing Stress and Relation to Faulting*, J. Geology *59*, 118–130.

YIN, J., *Détermination du Champ de Contrainte Régional à Partir de Mesures Hydrauliques et de Mécanismes au Foyer de Microséismes Induits*, Thèse de Doctorat de l'Univ. Paris VII et de l'Inst. Phys. Globe de Paris 1994.

YIN, J., and CORNET, F. H. (1994), *Integrated Stress Determination by Joint Inversion of Hydraulic Tests and Focal Mechanisms*, Geophys. Res. Lett. 29 (24) 2645–2648.

Received November 18, 1994, revised March 31, 1995, accepted April 10, 1995.